Supplementary Material: Meshfree *versus* grid-based Schrödinger solvers for modeling the interactions between free-electron wave packets and light

Mitja Funk,[1,*] Sebastian Merk,[2,†] Caroline Lasser,[2,‡] Marlis Hochbruck,[3,§] and Nahid Talebi[1,¶]

[1] *Institute for Experimental and Applied Physics, Kiel University, Leibnizstraße 19, 24118 Kiel, Germany*
[2] *Department of Mathematics, Technical University of Munich, Boltzmannstraße 3, 85748 Garching bei München, Germany*
[3] *Institute for Applied and Numerical Mathematics, Karlsruhe Institute of Technology, Englerstraße 2, 76131 Karlsruhe, Germany*

(Dated: July 3, 2026)

I. VECTOR POTENTIAL

For the stimulated Compton scattering benchmark, the optical fields are modeled as pulsed paraxial Gaussian beams following the formulation of Porras [1]. The total vector potential entering the ponderomotive interaction is written as

$$A_z(\mathbf{r},t) = \sum_{i=1}^{2} A^{(i)}(\mathbf{r},t), \tag{1}$$

where each contribution corresponds to one of the two laser pulses.

For beam i, the field envelope is chosen as

$$\psi^{(i)}(r_i,z_i,t_i') = \operatorname{sinc}\left[\frac{2}{\delta t^{(i)}}\left(t_i' - \frac{r_i^2}{2cq_i(z_i)}\right)\right] \times \frac{iz_R^{(i)}}{q_i(z_i)} \exp\left(-\frac{ik_0^{(i)} r_i^2}{2q_i(z_i)}\right), \tag{2}$$

with $\operatorname{sinc}(x) = \sin(\pi x)/(\pi x)$. The carrier wave number $k_0^{(i)}$, carrier frequency $\omega_0^{(i)}$, beam waist $a_0^{(i)}$, and Rayleigh range $z_R^{(i)}$ satisfy

$$k_0^{(i)} = \frac{\omega_0^{(i)}}{c}, \qquad z_R^{(i)} = \frac{k_0^{(i)}\left(a_0^{(i)}\right)^2}{2}. \tag{3}$$

The complex beam parameter is

$$q_i(z_i) = z_i + iz_R^{(i)}. \tag{4}$$

The coordinates in the local frame of beam i are defined as

$$z_i = x\cos\varphi_i + y\sin\varphi_i, \quad r_i = -x\sin\varphi_i + y\cos\varphi_i, \tag{5}$$

where z_i denotes the coordinate along the propagation direction and r_i the transverse coordinate. The retarded time is

$$t_i' = t - \frac{z_i}{c}. \tag{6}$$

Within the slowly varying envelope approximation, the vector potential of beam i is given by

$$A^{(i)}(r_i,z_i,t_i') = \frac{E_0^{(i)}}{\omega_0^{(i)}} \operatorname{Im}\Big(\psi^{(i)}(r_i,z_i,t_i') \times \exp\Big(i\omega_0^{(i)} t_i' + i\frac{\pi}{2}\Big)\Big), \tag{7}$$

where $E_0^{(i)}$ denotes the peak electric-field amplitude of beam i. The resulting vector potential is polarized along the out-of-plane direction and enters the effective ponderomotive potential used in the simulations.

II. CONVERGENCE

The convergence parameters for the split-step and TGWP methods are chosen such that while the reference (split-step) yields results with reasonable accuracy, the TGWP result converges with respect to the split-step result. The convergence is tested for the momentum space wave function after the interaction, since it is the central quantity of comparison discussed in this work. The relevant parameters are the real space grid spacing and time step for the split-step, the number of Gaussian trajectories, and the time step for TGWP. The trajectory convergence plots below were generated with the time-steps and Γ given in Tab. **??**. The time step convergence plots below were generated with 2^{15} trajectories for the Compton scattering and 2^{18} trajectories for the dipole potential.

The trajectory convergence in Fig. 1 (top) follows an empirical rate of $\mathcal{O}(N^{-0.8})$, lying between the $\mathcal{O}(N^{-1/2})$ rate of plain Monte Carlo sampling and the $\mathcal{O}(N^{-1})$ rate attainable with quasi-Monte Carlo sequences. The slopes indicated by the triangles in the trajectory-convergence plots are estimated from a corresponding self-convergence study, averaged over all shown curves. The convergence with respect to the time step in Fig. 1 (bottom) is

* funk@physik.uni-kiel.de
† s.merk@tum.de
‡ classer@tum.de
§ marlis.hochbruck@kit.edu
¶ talebi@physik.uni-kiel.de

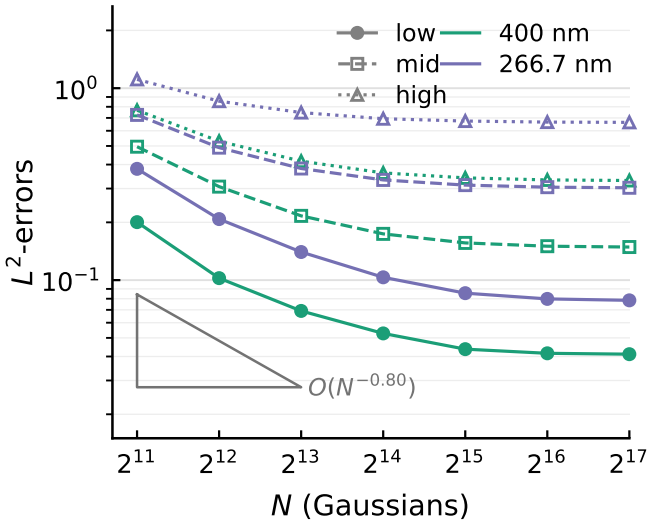

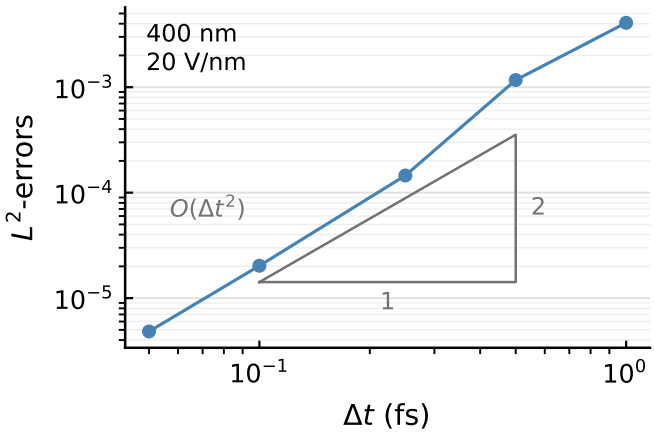

FIG. 1. Convergence of the TGWP momentum-space wave function for the stimulated Compton scattering. Top: convergence with the number of Gaussian trajectories N relative to the split-step reference, for the parameter combinations of Tab. III; low/mid/high corresponds to the strength of the potential. Bottom: self-convergence with the time step Δt for the set $\lambda_2 = 400\,\mathrm{nm}$, $E_0 = 20\,\mathrm{V/nm}$.

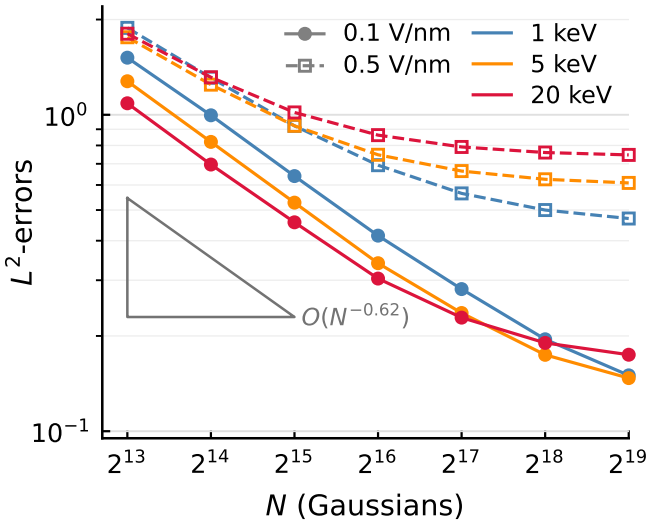

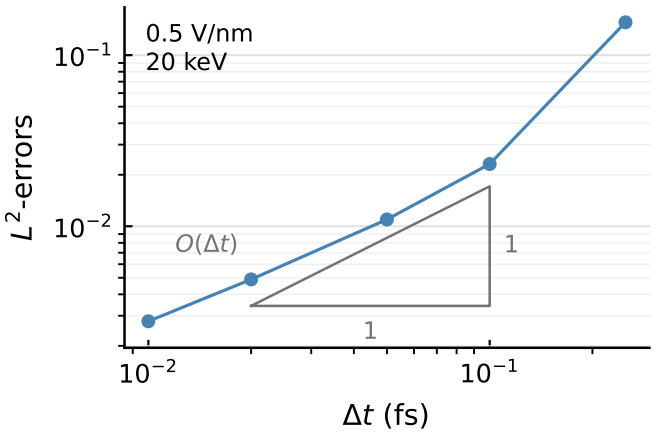

FIG. 2. Convergence of the TGWP momentum-space wave function for the dipole. Top: convergence with the number of Gaussian trajectories N relative to the split-step reference, for the parameter combinations of Tab. II. Bottom: self-convergence with the time step Δt for the representative set $E_0 = 0.5\,\mathrm{V/nm}$, $U_e = 20\,\mathrm{keV}$.

of second order, $\mathcal{O}(\Delta t^2)$, consistent with the Störmer–Verlet integrator used to propagate the trajectories.

For the dipole potential, the quasi-Monte Carlo sampling is less efficient at $\mathcal{O}(N^{-0.62})$. Moreover, the second-order convergence in the time step is lost (Fig. 2, bottom), since trajectories pass through the non-smooth part of the potential, violating the assumption of the error analysis of the Störmer–Verlet scheme. If we smooth the potential with a degree-5 Hermite interpolant on the interval $[0.8\,R,\, R]$, we obtain second-order convergence, as shown in Fig. 3; this approximation increases the L^2-error against the reference by less than 1%.

Based on these results, the calculations presented in the main text use $N = 2^{15}$ Gaussians for the stimulated Compton scattering and $N = 2^{18}$ for the dipole. At these values, the trajectory-sampling error has saturated, i.e., it is no longer reduced significantly by further increasing N, and constitutes the dominant contribution to the total error of the TGWP results. The time-stepping error at the employed step size is negligible in comparison and of similar size as the time-stepping error of the split-step reference itself.

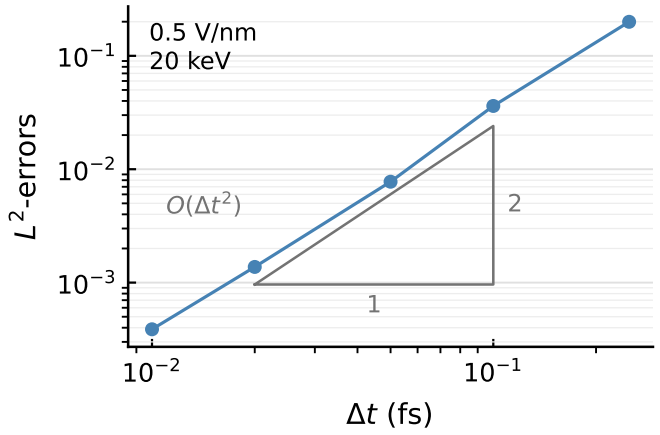

FIG. 3. Self-convergence with the time step Δt for the smoothed dipole potential ($E_0 = 0.5\,\mathrm{V/nm}$, $U_e = 20\,\mathrm{keV}$); second-order convergence is recovered.

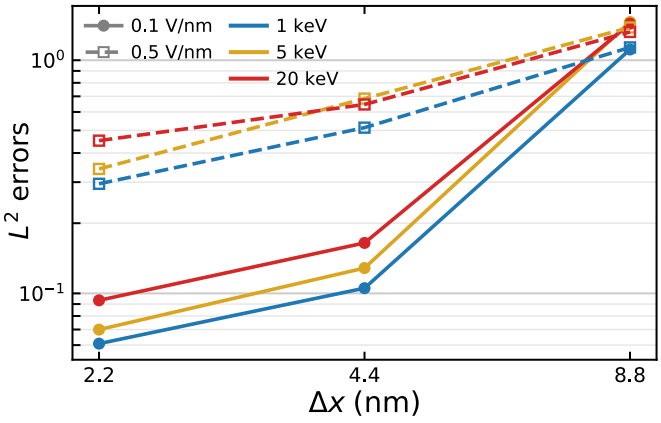

FIG. 4. Split step self-convergence for the dipole interaction data with respect to the grid spacing

III. WAVE FUNCTION SETS AFTER INTERACTION

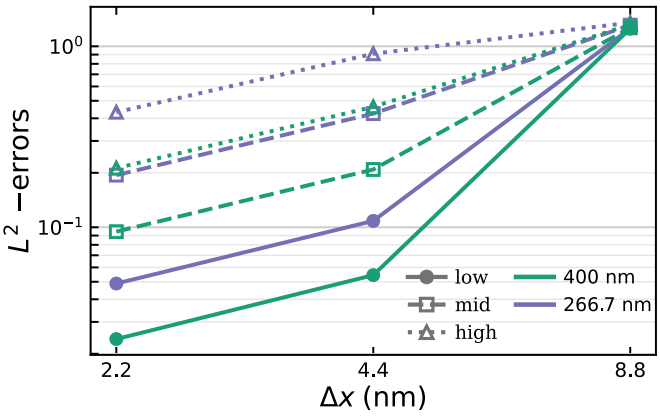

FIG. 5. Split step self-convergence for the stimulated Compton scattering data with respect to the grid spacing

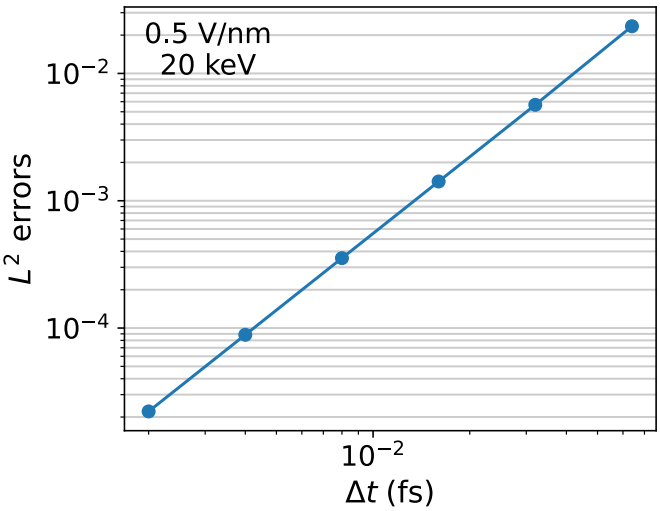

FIG. 6. Split step self-convergence for the dipole interaction data with respect to the time step

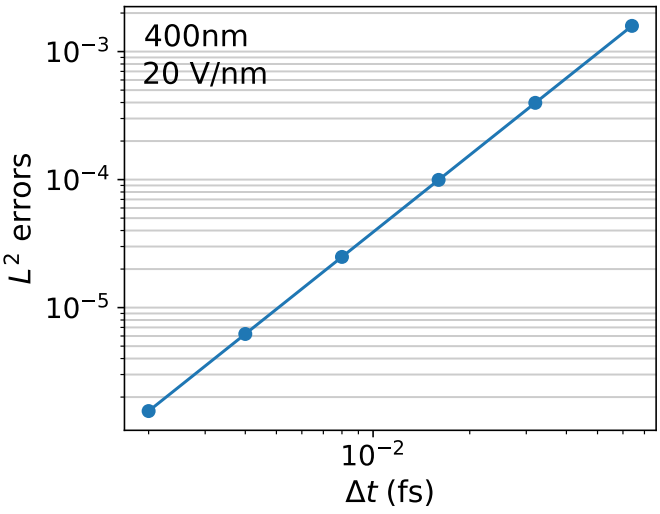

FIG. 7. Split step self-convergence for the stimulated Compton scattering with respect to the time step

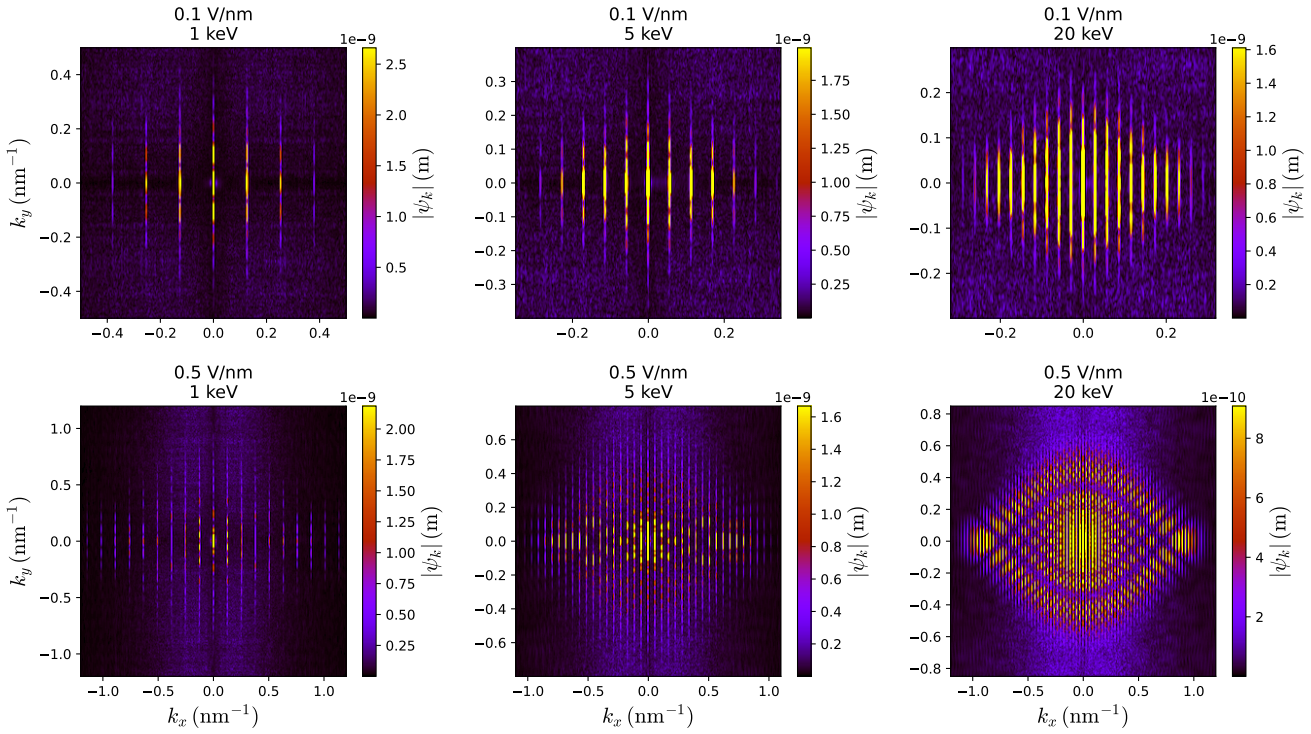

FIG. 8. Wave function absolutes after interaction for all considered parameter sets for the near-field case, corresponding to Fig. 3 of the main text. Only the TGWP data is shown. The parameter sets describe different interaction strengths resulting in different transverse and longitudinal momentum distributions after interaction.

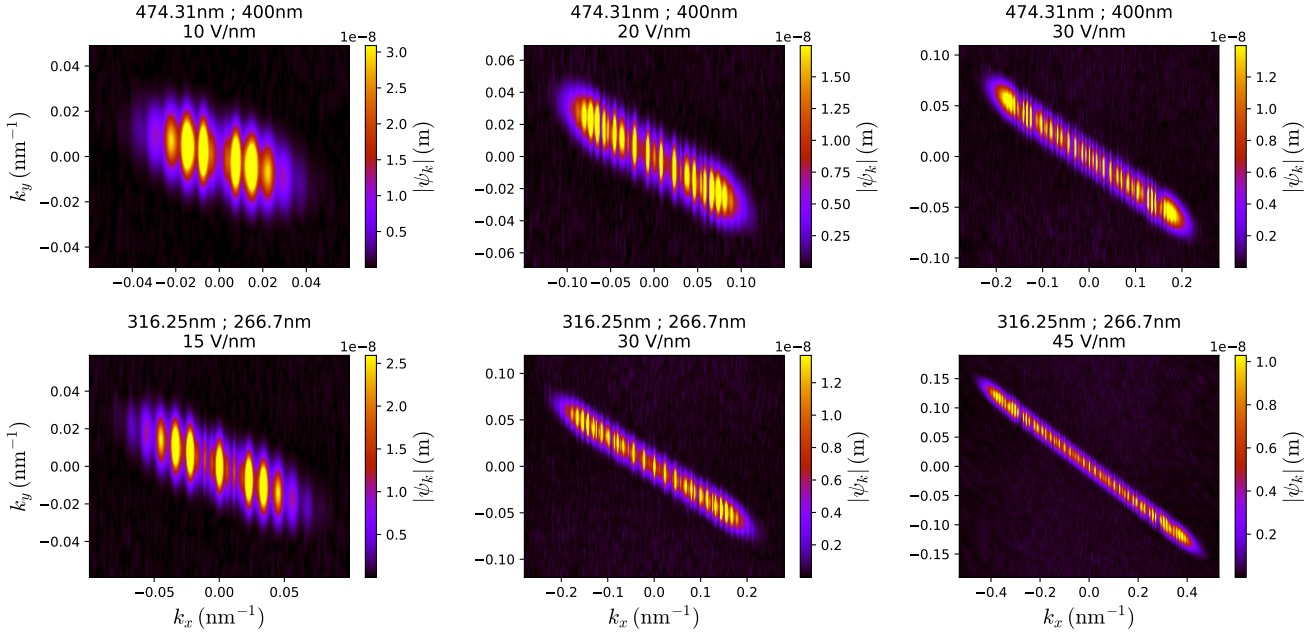

FIG. 9. Wave function absolutes after interaction for all considered parameter sets for the stimulated Compton case, corresponding to Fig. 5 of the main text. Only the TGWP data is shown. Changing the laser pulse wave lengths and field strengths changes the extent and internal structure of the wave function due to interference, while the momentum transfer remains mainly longitudinal.

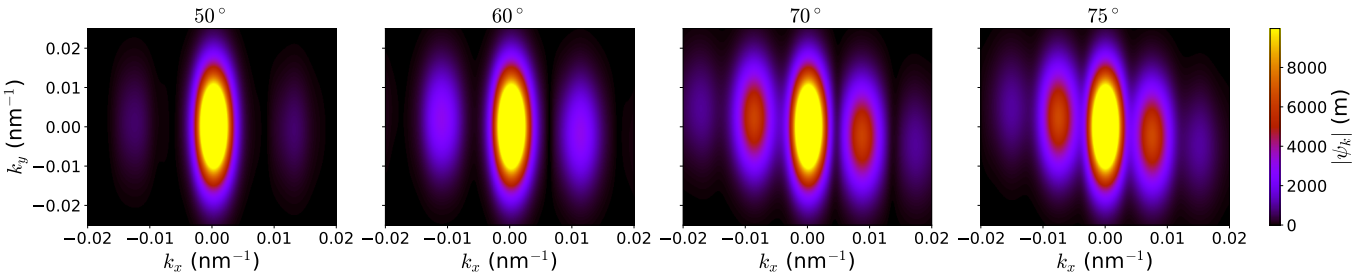

FIG. 10. Wave function absolutes for varying inclination beam angle for stimulated Compton scattering, corresponding to the left box of Fig. 6 of the main text. Deviations from the ideal phase-matching condition modify the recoil momentum and therefore shift the sideband positions. Due to the finite spatial and temporal extent of the optical pulse, phase matching possesses a finite tolerance, such that the interaction strength decreases continuously rather than vanishing abruptly as the mismatch increases.

[1] M. A. Porras, Phys. Rev. E **58**, 1086 (1998).